CHEMISTRY OF MATERIALS

Article

pubs.acs.org/cm

Facile Preparation of Monolithic $LiFePO_4$/Carbon Composites with Well-Defined Macropores for a Lithium-Ion Battery

George Hasegawa,*[,†] Yuya Ishihara,[‡] Kazuyoshi Kanamori,[†] Kohei Miyazaki,[‡] Yuki Yamada,[§] Kazuki Nakanishi,[†] and Takeshi Abe[‡]

[†]Department of Chemistry, Graduate School of Science, Kyoto University, Kitashirakawa, Sakyo-ku, Kyoto 606-8502, Japan

[‡]Department of Energy and Hydrocarbon Chemistry, Graduate School of Engineering, Kyoto University, Kyoto daigaku-Katsura, Nishikyo-ku, Kyoto 615-8530, Japan

[§]Department of Chemical System Engineering, Graduate School of Engineering, The University of Tokyo, Hongo, Bunkyo-ku, Tokyo 113-8656, Japan

Supporting Information

ABSTRACT: A novel and facile method for the preparation of monolithic $LiFePO_4$/carbon composites with well-defined macropores has been developed. The precursor macroporous gels consisting of inorganic networks as well as organic polymers were fabricated by the epoxide-mediated sol–gel method accompanied by phase separation. The inorganic–organic hybrid gels were calcined under an inert atmosphere, resulting in $LiFePO_4$/carbon monoliths. The influence of the starting compositions on the gel morphologies has been investigated, and the constituents of the gel network were discussed. The reaction mechanism of the crystallization of $LiFePO_4$ from green bodies during calcination has also been investigated by thermal analysis, X-ray diffraction, and Raman scattering. In addition, the electrochemical properties of the resultant $LiFePO_4$/carbon composites were examined by the charge–discharge test.

KEYWORDS: *olivine, cathode materials, macroporous monoliths, sol–gel reaction, phase separation*

1. INTRODUCTION

Lithium (Li) secondary batteries have become a ubiquitous power source for various applications including not only portable energy storage devices for cellular phones and lap-top computers but also large-scale ones for electric vehicles and hybrid electric vehicles.[1−6] Wide-spread applications demand low cost, high reversibility, and safety for rechargeable Li-ion batteries. From these viewpoints, the olivine-type materials have been extensively studied as promising cathode materials. Especially, $LiFePO_4$ is one of the most promising cathode materials because of its high theoretical capacity (170 mAh g^{-1}), suitable thermal stability, low environmental impact, and low cost.[7−17] As is well-known, the main issues of $LiFePO_4$ are its low Li-ion diffusion rate and poor intrinsic electronic conductivity, which reduce the capacity of the battery. Many efforts have been made to solve these issues, and it was revealed that the small particle size of $LiFePO_4$ is helpful in increasing the Li-ion diffusion rate[10,11] and that coating of the $LiFePO_4$ particles with carbon can improve the electric conductivity.[12−15] Doping with supervalent cations, such as Mg, Al, Ti, and Nb, is useful for improvement of the electric conductivity as well.[16]

Recently, porous electrode materials have attracted more and more attention because an increase in the electrode/electrolyte interfaces improves the electrochemical properties by enhancing the charge transport.[18−24] In particular, hierarchically porous materials that contain micro-, meso-, and macropores are desirable for a further improvement in the properties of the electrodes. The presence of micropores provides high specific surface area, increasing the interfacial area between the electrode and electrolyte, while that of meso- and macropores allows the efficient mass transport of the electrolyte throughout the electrode. Doherty et al. prepared hierarchically porous monolithic $LiFePO_4$/carbon composites by impregnating $LiFePO_4$ onto porous carbon monoliths, which were produced as replicas of porous silica monoliths synthesized via the sol–gel method accompanied by spinodal decomposition.[23] However, starting from the silica monoliths, their process requires many laborious steps to obtain the final composite product. In addition, the macropores of the resultant composites are mostly filled with the impregnated $LiFePO_4$ crystallites, which deteriorate the electrochemical performances.

In this paper, we demonstrate the novel and facile preparation of porous $LiFePO_4$/carbon composites for Li-ion battery applications. The synthesis approach is based on the sol–gel method reported by Tokudome et al.[25] They have successfully prepared macroporous Al_2O_3 monoliths as well as other complex oxides from the solution of metal salts.[25−27]

Received: July 26, 2011
Revised: October 14, 2011
Published: November 4, 2011

Table 1. Starting Compositions Investigated in This Study[a]

	Li_2CO_3 /mmol	$FeCl_3 \cdot 6H_2O$/mmol	H_3PO_4 /mmol	H_2O/mL	PO/mmol	PVP/g	PEO/g
LFP8-16-8-0	4.0	8.0	8.0	8.0	16	0.80	0
LFP8-16-8-16	4.0	8.0	8.0	8.0	16	0.80	0.16
LFP8-16-8-20	4.0	8.0	8.0	8.0	16	0.80	0.20
LFP8-16-8-24	4.0	8.0	8.0	8.0	16	0.80	0.24
LFP8-16-8-40	4.0	8.0	8.0	8.0	16	0.80	0.40
LFP8-15-8-20	4.0	8.0	8.0	8.0	15	0.80	0.20
LFP8-17-8-20	4.0	8.0	8.0	8.0	17	0.80	0.20
LFP8-18-8-20	4.0	8.0	8.0	8.0	18	0.80	0.20
LFP8-16-4-20	4.0	8.0	8.0	8.0	16	0.40	0.20
LFP8-16-6-20	4.0	8.0	8.0	8.0	16	0.60	0.20
LFP8-16-10-20	4.0	8.0	8.0	8.0	16	1.00	0.20

[a]Sample codes were named as LFP*w-x-y-z*, where *w*, *x*, *y*, and *z* correspond to the amount of H_2O, PO, PVP, and PEO, respectively.

The sol−gel reaction is triggered by an increase in the pH induced by the ring-opening reaction of propylene oxide, which acts as a proton scavenger.[28−30] The well-defined macropores were tailored by fixing the cocontinuous structure, which is formed in the course of spinodal decomposition, by the sol−gel transition.[31] This synthesis process of macroporous metal oxide is promising because the sources of metal salts are inexpensive and more easily handled compared to the corresponding metal alkoxides. In this work, macroporous $LiFePO_4$/carbon composites have been successfully prepared from inorganic−organic hybrid gels, which were synthesized by the aforementioned sol−gel method accompanied by phase separation. In order to obtain the porous hybrid gels, we have used two kinds of polymers: poly(ethylene oxide) (PEO) and poly(vinylpyrrolidone) (PVP). PEO acts as a phase separation inducer, while PVP, which was known as the nitrogen-doped carbon precursor,[32] is expected to act not only as a carbon precursor but also as a reducing agent of iron species.[33,34] Besides, PVP and the resulting carbonaceous species, which are finely dispersed in the gel network, are expected to suppress the excessive crystal growth of $LiFePO_4$ by separating crystallites during calcination. In this report, the effects of the starting composition on the gel morphology and the reaction mechanism from green bodies to $LiFePO_4$/carbon composites were investigated. In addition, the obtained $LiFePO_4$/carbon composites were applied to the electrodes of the Li-ion battery. The effects of the calcination temperature on the electric performance were investigated by the charge−discharge measurement.

2. EXPERIMENTAL PROCEDURES

2.1. Materials. $FeCl_3 \cdot 6H_2O$, H_3PO_4 (85 wt % in H_2O), propylene oxide (PO), poly(vinylpyrrolidone) (PVP; M_w = 10 000), and poly(ethylene oxide) (PEO; M_w = 100 000) were purchased from Sigma-Aldrich Co. (Madison, WI). Li_2CO_3 was purchased from Wako Pure Chemical Industries, Ltd. (Osaka, Japan). All reagents were used as received. Distilled water was used in all experiments.

2.2. Sample Preparation. The starting compositions were listed in Table 1. In a typical synthesis, a given amount of $FeCl_3 \cdot 6H_2O$ was dissolved in H_2O in a glass tube. Subsequently, Li_2CO_3 was added to the resultant homogeneous yellow solution with vigorous stirring. Then, PEO, PVP, and H_3PO_4 were added in sequence. The molar ratio of Li/Fe/PO_4 was fixed as 1:1:1. After stirring at room temperature for 1 h, the resultant transparent yellow solution was cooled to 0 °C in an ice/water bath and PO was added slowly (about 1 mL min^{-1}) with vigorous stirring. After mixing for 30 s, the obtained homogeneous solution was degassed by ultrasonication for 30 s in order to remove bubbles, followed by gelation. After gelation, the obtained wet gels were aged at 40 °C for 1 h and dried at 40 °C. The sample codes were given as LFP*w-x-y-z*, where *w*, *x*, *y*, and *z* are assigned as the amount of H_2O, PO, PVP, and PEO. The resultant xerogels were subsequently heat-treated at various temperatures for 2 h with a heating rate of 5 °C min^{-1} in the N_2 stream at a rate of 1 L min^{-1} in an electric furnace, which had been purged with N_2 in advance to completely remove air inside the pores of the samples.

2.3. Characterization. The change of the pH value during the sol−gel reaction was measured at 0 °C using a pH meter F-21 (HORIBA, Ltd., Kyoto, Japan). The pH measurement started as soon as the addition of PO started, and the time for the addition of PO was 30 s. Observation of the microstructures of the fractured surfaces of the samples and elemental analysis were conducted under scanning electron microscopy−energy-dispersive X-ray spectroscopy (SEM-EDS; JSM-6060S, JEOL, Japan) and field-emission SEM (FE-SEM; JSM-6700F, JEOL, Japan). The crystal structure was confirmed by powder X-ray diffraction (XRD; RINT Ultima III, Rigaku Corp., Japan) using Cu Kα (λ = 0.154 nm) as an incident beam. Raman spectra of the $LiFePO_4$/carbon composites were measured using a Jobin-Yvon T-6400 spectrometer (HORIBA, Ltd.). The incident light used for the experiments was the 514.5 nm Ar line of the laser source (GLG3260, NEC Corp., Tokyo, Japan). Thermogravimetry (TG) and differential thermal analysis (DTA) measurements were performed by Thermo plus TG 8120 (Rigaku Corp., Tokyo, Japan) at a heating rate of 5 °C min^{-1} while continuously supplying air or Ar at a rate of 100 mL min^{-1}. A mercury porosimeter (Pore Master 60-GT, Quantachrome Instruments, Boynton Beach, FL) was used to characterize the macropores of the samples, while a N_2 adsorption−desorption apparatus (Belsorp mini II, Bel Japan Inc., Osaka, Japan) was employed to characterize the meso- and micropores of the samples. Helium pycnometry (Accupyc 1330, Micromeritics, Norcross, GA) was employed to determine the skeletal density of the heat-treated samples. Before N_2 adsorption−desorption measurement and helium pycnometry, the sample was degassed at 200 °C under vacuum. The bulk density of each sample was measured by mercury porosimetry. The porosity (%) of each sample was calculated as $[(1 - \rho_b)/\rho_s] \times 100$, where ρ_b and ρ_s are assigned as the bulk and skeletal densities, respectively.

2.4. Electrochemical Analysis. The $LiFePO_4$ electrode slurries comprised 85% active material, 10% acetylene black, and 5% poly(vinylidene fluoride) binder, in the solvent *N*-methyl-2-pyrrolidone (Tokyo Chemical Ind. Co., Ltd., Tokyo, Japan). The electrode slurry was coated onto the Al foil. The electrode was then dried under vacuum at 120 °C for more than 24 h. The electrodes were tested in a three-electrode cell consisting of a 1 M $LiPF_6$ electrolyte in 1:1 (v/v) ethylene carbonate/diethyl carbonate (Kishida Chemical Co., Ltd., Osaka, Japan) and Li metal as both counter and reference electrodes. The electrochemical testings were carried out using an HJ1001SD8 potentiostat (Hokuto-Denko Inc., Tokyo, Japan). For consistency, the currents were calculated on the active material only, which was determined by TG analysis. The constant current charge−discharge tests were carried out with 2.0 and 4.5 V cutoff potentials.

dx.doi.org/10.1021/cm2021438 | *Chem.Mater.* 2011, 23, 5208−5216

3. RESULTS AND DISCUSSION

3.1. Preparation of Green Bodies by the Sol–Gel Method. In this study, we utilized a low-cost and versatile sol–gel method with ionic precursors and epoxides to obtain green bodies of $LiFePO_4$/carbon composites.[29,30] In order to obtain the information on the formation of the gel network, the change in the pH value after the addition of PO was investigated as shown in Figure 1a. The pH value before the addition of PO was −0.14. Here, the addition of PO started at $t = 0$ s and ended at $t = 30$ s. After the addition of PO, the pH value increased dramatically in a few minutes and the solution temperature increased in several degrees because of the ring-opening reaction of PO, as shown in Figure 1b. The gelation took place at pH values of 0.85–0.90. Even after gelation, the pH gradually increased with time and reached 1.44 in 2 h. According to the previous report,[30] Fe_2O_3 gels were formed at the pH value of ∼5.2, at which large cationic oligomers of iron(III) hydroxy and oxohydroxy species exist, when PO was added to the $FeCl_3$ aqueous solution. On the other hand, in this study, the gel networks are mainly composed of amorphous $FePO_4$, which is poorly soluble in water.[35] The gelation time ranged from a couple of minutes to an hour depending on the starting composition. The gelation time can be controlled to some extent by varying the amount of PO; the decrease in the amount of PO extends the gelation time because the pH increases more slowly.

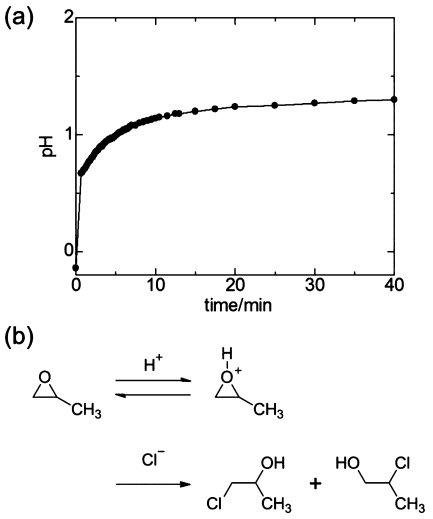

Figure 1. (a) Change in the pH value after the addition of epoxide and (b) the ring-opening reaction of PO.

In order to keep the stoichiometry, the resultant wet gels were subsequently dried at 40 °C without washing. When the gels were dried in a closed container with a pinhole, crack-free dried gels could be obtained, as shown in Figure 2a. The macroporous structures of the dried gels with varied amounts of PEO are shown in Figure 2b–f. It is found that almost no phase separation took place and the transparent gel with no macropores was obtained when PEO was not added, as shown in Figure 2b. As shown in Figure 2c–f, the macroporous structure becomes coarser when the amount of PEO increased, and the gel morphology finally became particle aggregates with the large amount of PEO. In the case of the sol–gel method accompanied by phase separation, the morphologies in submicrometer-to-micrometer scale of the gels are formed by fixing ("freezing") the morphologies that are formed during the phase separation.[31] The enlargement of the domain size derived from the higher phase-separation tendency between the gel and fluid phases. In this sol–gel system, PEO is deduced to be mostly distributed to the fluid phase like the sol–gel system of the Al_2O_3 monoliths,[25] and the decreasing compatibility between the growing small $FePO_4$ and PEO led to phase separation.

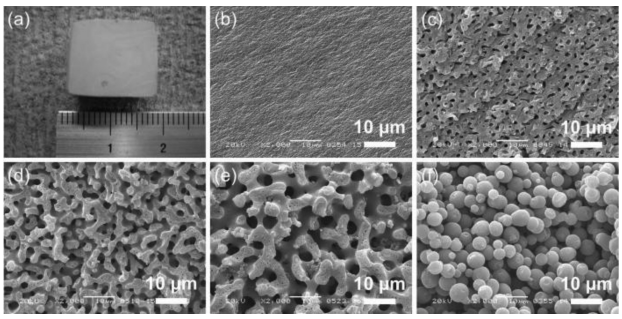

Figure 2. (a) Appearance of the resultant xerogel and the macroporous structure of the xerogels with varied amounts of PEO: (b) LFP8-16-8-0, (c) LFP8-16-8-16, (d) LFP8-16-8-20, (e) LFP8-16-8-24, and (f) LFP8-16-8-40.

The effect of the amount of PO on the gel morphologies was also investigated, as shown in Figure 3. The increase in the amount of PO effectively shortens the gelation time because PO accelerates the pH increase as described above. As shown in the caption of Figure 3, the amount of PO has a potent influence on the gelation time. The macroporous structure became finer with an increase in the amount of PO because the timing of the sol–gel transition during the phase separation became much earlier, even when the amount of PO is slightly increased. This indicates that the compatibility between the gel and fluid phases is hardly influenced by the amount of PO.

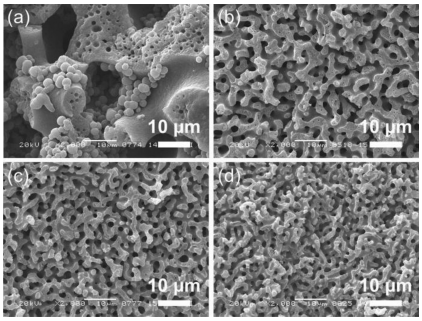

Figure 3. Macroporous structure of the xerogels with varied amounts of PO: (a) LFP8-15-8-20; (b) LFP8-16-8-20; (c) LFP8-17-8-20; (d) LFP8-18-8-20. The gelation time of each sample was (a) 20, (b) 7, (c) 4, and (d) 3 min.

Figure 4 shows the gel morphologies with varied amounts of PVP. By a comparison of parts c and d of Figure 4, it is obvious that the volume fraction of [gel phase]/[fluid phase] increased as the amount of PVP increased because the interconnected porous structure changes to the isolated porous structure. This fact indicates that PVP is mainly distributed to the gel phase, which is desirable because PVP should act as the carbon precursor. The similar behavior of changing gel morphologies with an increase in the amount of PVP can be observed when the amount of H_2O decreased, as shown in Figure S1 in the

dx.doi.org/10.1021/cm2021438 | Chem.Mater. 2011, 23, 5208–5216

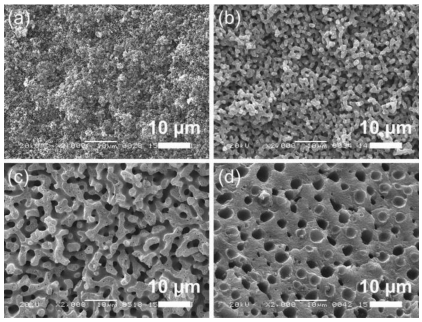

Figure 4. Macroporous structure of the xerogels with varied amounts of PVP: (a) LFP8-16-4-20; (b) LFP8-16-6-20; (c) LFP8-16-8-20; (d) LFP8-16-10-20.

Supporting Information. The decrease in the amount of H_2O naturally leads to an increase in the ratio of [gel phase]/[fluid phase]. As a result, the gel morphology changed from an interconnected porous structure to an isolated porous structure. When a comparison is made among parts a–c of Figure 4, the morphology changed from the nanoporous structure to the macroporous structure and the macropores became larger with an increase in the amount of PVP. This is because the increase in the ratio of [gel phase]/[fluid phase] brings about an increase in the phase-separation tendency. As mentioned above, the phase-separation tendency depends on the compatibility between the gel phase and the PEO-rich fluid phase. When the amount of PEO is fixed, the increase in the concentration of the gel phase with increasing PVP naturally enhances the phase-separation tendency.

An appropriate choice of the starting composition based on the above information allows the preparation of the gels with well-defined macropores obtained with varied amounts of PVP by adjusting the amounts of the other components, as shown in Figure S2 in the Supporting Information. In addition, we can also control the macropore size of each gel with varied amounts of PVP by varying the amount of PEO.

3.2. Characterization of $LiFePO_4$/Carbon Composites. The typical sample with well-defined macropores (LFP8-16-8-20) was used as a green body for preparing $LiFePO_4$/carbon composites unless otherwise noted. Figure 5 shows the XRD patterns and the Raman spectra of the as-dried and calcined samples. It is found from the XRD patterns that the as-dried sample and the sample calcined at below 400 °C were amorphous and the green bodies changed to $LiFePO_4$ when calcined at over 500 °C. In addition, no peaks attiributed to the byproduct such as Li_3PO_4, $Li_3Fe_2(PO_4)_3$, Fe_3P, and iron oxides were observed even when iron(III) salt was used as the iron source. In the Raman spectra, two obvious bands at ~1350 and ~1600 cm^{-1}, which are attirbuted to the D band (disordered carbon, sp^3) and the G band (graphite, sp^2), can be observed. These results indicate that the obtained samples calcined at above 600 °C were $LiFePO_4$/carbon composites. The small peak at ~1130 cm^{-1} is presumably attributed to noise or the C–C stretching modes of carbonaceous species.[36] The ν_4, ν_1, ν_3, and ν_3 intramolecular stretching modes of $(PO_4)^{3-}$ units give rise to scattering at 620, 940, 986, and 1058 cm^{-1}, respectively.[10,37] In Figure 5b, peaks at around 950 cm^{-1} are observed in all of the spectra and the peak intensity increased when the calcination temperature was 900 °C. In addition, the Raman spectrum of the sample calcined at 900 °C includes the other peaks of $(PO_4)^{3-}$ units at 630, 1000, and 1070 cm^{-1}.

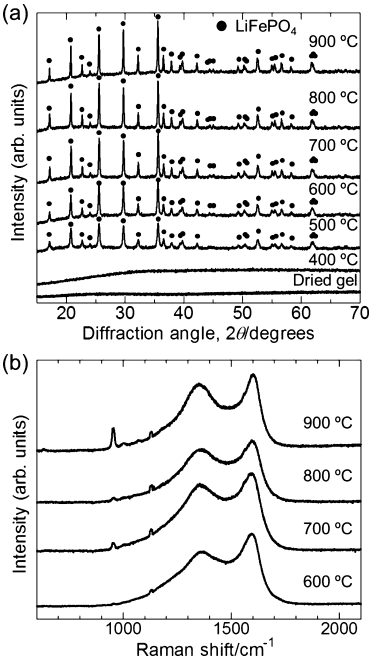

Figure 5. (a) XRD patterns and (b) Raman spectra of the calcined samples.

This indicates that the $LiFePO_4$ crystallites of the samples calcined below 800 °C were well-coated with carbon, while those of the sample calcined at 900 °C were poorly coated with carbon.[37]

In order to investigate the reaction during calcination, TG–DTA measurements of the green bodies with and without polymers (PEO and PVP) under an air or Ar atmosphere were carried out, as shown in Figure 6. In the case of the sample with

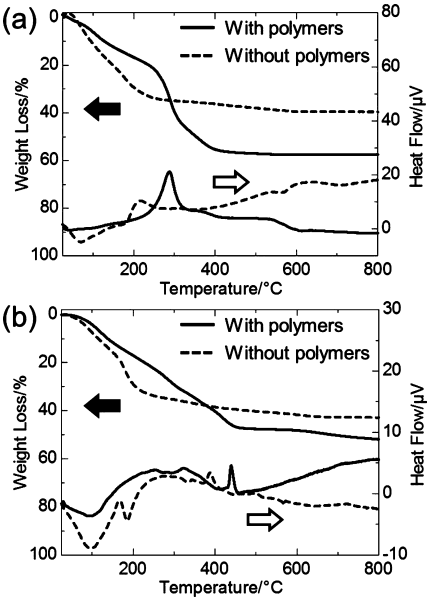

Figure 6. TG–DTA analysis results of the green bodies prepared with and without polymers (PEO and PVP) conducted under an air atmosphere (a) and an Ar atmosphere (b).

polymers, a strong exothermic peak appeared between 250 and 350 °C in the DTA curve and a steep reduction of the sample weight is observed at around 300 °C in the TG curve, which are

dx.doi.org/10.1021/cm2021438 | Chem.Mater. 2011, 23, 5208–5216

attributed to pyrolysis of the polymers. Weight loss is also observed below 250 °C, which appears in the sample without any polymers as well. This is deduced to be derived from removal of Cl-containing species from the samples. The obtained gel networks include a lot of Cl^- ions derived from $FeCl_3$. These species presumably coordinate to Fe or play the role of charge compensation in the networks. In the case of an Ar atmosphere, weight loss from 200 to 400 °C is attributed to removal of Cl-including species as well as pyrolysis of the polymers (mainly PEO), which can be confirmed by the EDX analysis results, as shown in Figure S3 in the Supporting Information. The peak derived from Cl Kα dramatically decreases between 200 and 400 °C. The exothermic peak can be observed at around 450 and 400 °C in the samples with and without polymers, respectively. Taking into account that crystallization of the sample with polymers took place between 400 and 500 °C, as shown in Figure 5, the exothermic peak at around 450 °C can be attributed to crystallization of $LiFePO_4$. Therefore, reduction from Fe^{III} to Fe^{II} occurred below 450 °C.

We also investigated the crystallization behavior of the sample without any polymers, as shown in Figure S4 in the Supporting Information. The XRD patterns show the peaks attributed to $LiFePO_4$ in the sample calcined at 400 °C, even though the sample calcined at 400 °C was amorphous starting from the green body with polymers. This result agrees with the TG–DTA result under an Ar atmosphere, and the exothermic peak at around 400 °C in the broken line can also be attributed to crystallization of $LiFePO_4$. It can be deduced that reduction from Fe^{III} to Fe^{II} was induced not only by the polymers but also by other components such as Cl^- ions upon oxidation. The higher crystallization temperature in the case of the sample with polymers is presumably caused by interaction between polymers, especially PVP, and metal ions through O atoms. Crystallization to $LiFePO_4$ did not take place before pyrolysis of the polymers, releasing metal ions. Because decomposition of pyrrolidone fragments generating carbonaceous species starts at 400 °C,[38] the green bodies with polymers needed higher temperature to crystallize into $LiFePO_4$. This assumption agrees with the fact that the exothermic behavior started at the temperature at which the obvious weight loss had stopped in the case of the sample with polymers, as shown in Figure 6b.

The appearance of $LiFePO_4$/carbon composites calcined at 800 °C and the macroporous morphologies of the calcined samples are shown in Figure 7. The black crack-free monolith

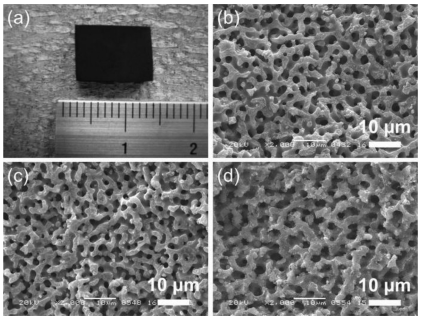

Figure 7. (a) Appearance of the monolithic $LiFePO_4$/carbon composite and the macroporous structure of the samples calcined at different temperatures: (b) 600 °C; (c) 800 °C; (d) 900 °C.

can be obtained after calcination under an inert atmosphere, as shown in Figure 7a. The macroporous structure was retained after calcination below 800 °C. In the case of the sample calcined at 900 °C, although the macroporous structure was partly retained, as shown in Figure 7d, the interconnected macropores had collapsed in some regions. The sample melted when it was calcined at 1000 °C because the melting point of $LiFePO_4$ is lower than 1000 °C.[39] As shown in Figure 8, the

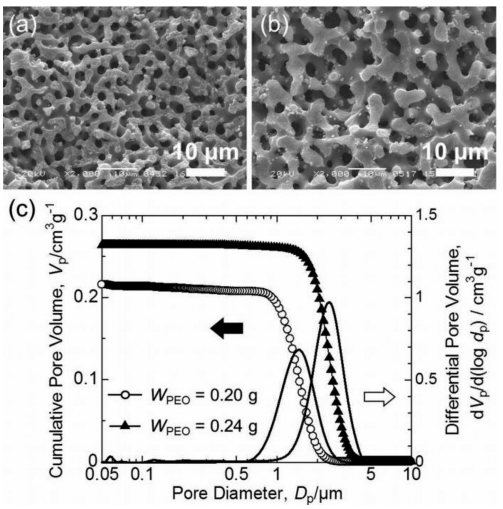

Figure 8. Macroporous structure of the samples calcined at 600 °C from the green bodies with different macropore sizes: (a) LFP8-16-8-20; (b) LFP8-16-8-24. (c) Pore-size distributions of the samples in parts a and b.

macropore diameter of $LiFePO_4$/carbon composites can be changed using the green bodies with different macropore sizes, which were controlled by varied amounts of PEO in the starting composition. Mercury porosimetry analysis revealed that the macropore size in each calcined sample possessed a sharp distribution, as shown in Figure 8c.

Figure 9 displays the finer images of the cross section of the skeleton, which constitutes the interconnected macroporous structure. The skeleton of the sample calcined at 400 °C, which was amorphous, is composed of several tens of nanometers of grains. The skeletons of the samples calcined above 600 °C include two different types of parts. One is a smooth part, which may be attributed to $LiFePO_4$ crystallites, and the other is a rough part, including nanometer-sized pores, which may be attributed to carbon derived from PVP. Besides, it is observed that the skeleton of the sample calcined at 900 °C is mainly composed of $LiFePO_4$ crystallites and only a small amount of carbons attach to the surface of the skeleton. The TEM images of the calcined samples can support this assumption, as shown in Figure 10. The carbon parts of the sample are shown as relatively light, and the relatively dark part corresponds to $LiFePO_4$ crystallites, which contain elements with higher atomic number. The relatively light region has a crooked structure, which corresponds to the rough part in the FE-SEM images of Figure 9. It is also found that the $LiFePO_4$ crystallites and carbon were well-mixed on the scale of several hundreds of nanometers in the $LiFePO_4$/carbon composites. The micro- and mesoporous properties of the $LiFePO_4$/carbon composites calcined at different temperatures were investigated by N_2 adsorption–desorption measurement, as shown in Figure 11 and Table 2. The uptake at very low relative pressure is derived from the existence of micropores of carbon. It is found that the calcined samples, except for the sample calcined at 900 °C,

dx.doi.org/10.1021/cm2021438 | Chem.Mater. 2011, 23, 5208–5216

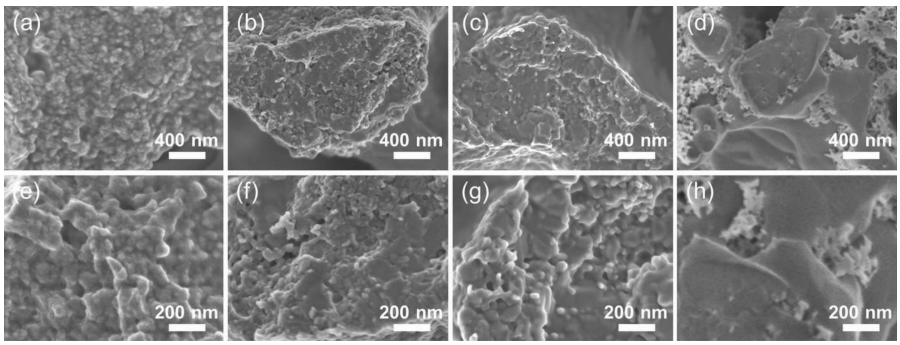

Figure 9. Morphologies of the cross section of the skeletons calcined at different temperatures: (a and e) 400 °C; (b and f) 600 °C; (c and g) 800 °C; (d and h) 900 °C.

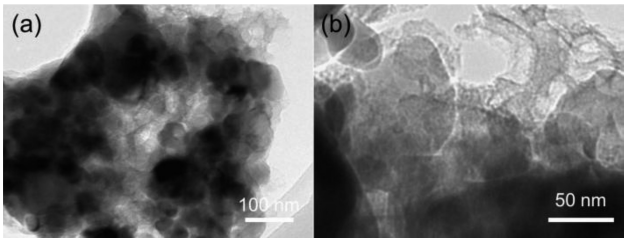

Figure 10. TEM images of the resultant $LiFePO_4$/carbon composites calcined at 800 °C.

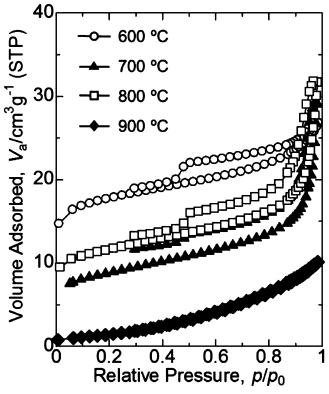

Figure 11. N_2 adsorption−desorption isotherms of the $LiFePO_4$/carbon composites calcined at different temperatures.

possessed micropores, and the specific surface area is ~68 m^2 g^{-1}. From 600 to 700 °C, the specific surface area decreases with increasing calcination temperature. On the other hand, the specific surface area of the sample calcined at 800 °C is higher than that of the sample calcined at 700 °C. The specific surface area decreases upon elevation of the calcination temperature because of shrinkage and a decrease of the carbon content. However, thermal activation by the small amount of oxidative species in the furnace takes place above 800 °C, which increases the amount of micropores as well as the specific surface area.[40] Because the skeleton is mostly composed of relatively large $LiFePO_4$ crystallites and there is only a small amount of carbon, as shown in Figure 9d, the mesopore volume as well as the micropore volume of the sample calcined at 900 °C is very small. The uptake at higher relative pressure is derived from mesopores in the samples. The porous structures that are observed in Figure 9f,g can be detected as a steep uptake at the region where the relative pressure is close to unity. In the case of the sample calcined at 600 °C, the pore size in the skeleton was larger than 50 nm, which is evidenced by the continuous uptake at this region. The bulk and skeletal densities as well as porosities of the calcined samples are also shown in Table 2. With increasing calcination temperature, both the skeletal and bulk densities increased and the skeletal density approached the ideal density of $LiFePO_4$ (3.6 g cm^{-3}). The resultant $LiFePO_4$/carbon composites have more than 50% porosity.

The TG curves of the $LiFePO_4$/carbon composites under an air atmosphere are shown in Figure 12. The decrease in the sample weight is attributed to pyrolysis of carbon, whereas the increase in the sample weight is caused by oxidation of $LiFePO_4$ as in the following reaction, which was confirmed by the XRD measurement, as shown in Figure S5 in the Supporting Information.

$$12LiFePO_4 + 3O_2 \rightarrow 4Li_3Fe_2(PO_4)_3 + 2Fe_2O_3$$

Taking this reaction into consideration, the carbon content of the calcined sample can be calculated from the TG results, as described in Table 3. It is found that the carbon content in the $LiFePO_4$/carbon composites decreased as the calcination temperature increased. In particular, the carbons in the sample calcined at 900 °C were only 6.8% of whole sample mass. This result agrees with the FE-SEM observation, as shown in Figure 9d,h. Besides, the obvious weight increase is observed

Table 2. Pore Characteristics and Crystallite Sizes of the $LiFePO_4$/Carbon Composites Calcined at Different Temperatures

calcination temperature/°C	S_{BET}/m^2 g^{-1}	V_p[a]/cm^3 g^{-1}	ρ_s[b]/g cm^{-3}	ρ_b[c]/g cm^{-3}	porosity[d]/%	crystallite diameter[e]/nm
600	68	0.042	3.09	1.38	55	50
700	33	0.045	3.10	1.39	55	50
800	44	0.049	3.25	1.51	54	50
900	4.8	0.016	3.45	1.71	50	70

[a]Micro- and mesopore volume obtained by N_2 absorption isotherms at $p/p_0 = 0.99$. [b]Skeletal density measured by helium pycnometry. [c]Bulk density measured by mercury porosimetry. [d]Calculated by $[(1 - \rho_b)/\rho_s] \times 100$. [e]Calculated using the XRD peak at $2\theta = 17°$ [$LiFePO_4$ (200) diffraction peak] by Scherrer's equation.

dx.doi.org/10.1021/cm2021438 | Chem.Mater. 2011, 23, 5208–5216

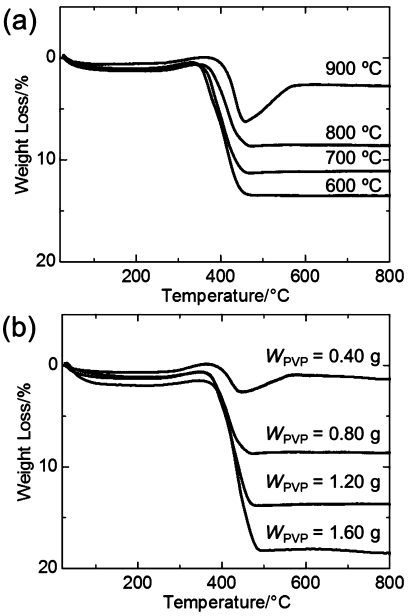

Figure 12. TG curves of the $LiFePO_4$/carbon composites calcined at different temperatures (a) and samples calcined at 800 °C from the green bodies prepared with varied amounts of PVP (b) under an air atmosphere.

Table 3. Carbon Contents of the Samples

calcination temperature[a]/°C	carbon content/%	W_{PVP}[b]/g	carbon content/%
600	17	0.40	5.1
700	14	0.80	12
800	12	1.20	17
900	6.8	1.60	20

[a]Using sample LFP8-16-8-20 (W_{PVP} = 0.80 g) as the green body. [b]Calcined at 800 °C for 30 min under an Ar atmosphere; LFP6-14.5-4-22 (W_{PVP} = 0.40 g), LFP8-16-8-20 (W_{PVP} = 0.80 g), LFP10-17-12-20 (W_{PVP} = 1.20 g), and LFP12-20-16-28 (W_{PVP} = 1.60 g).

only in the TG curve of the sample calcined at 900 °C in Figure 12a, although there is only a small weight increase in the case of the samples calcined below 800 °C. In other words, oxidation of $LiFePO_4$ took place simultaneously with the burnoff of carbons in the case of the samples calcined below 800 °C, whereas oxidation took place at higher temperature in the case of the sample calcined at 900 °C. This tendency is also observed in Figure 12b; the obvious weight increase is observed only in the TG curve of the sample of W_{PVP} = 0.40 g. This is presumably because of the larger $LiFePO_4$ crystallite size and the small amount of carbons. The larger crystallites are less oxidized. Meanwhile, when the sample skeleton is composed of a mixture of $LiFePO_4$ crystallites and carbons, pores are generated in the skeletons when the carbons are removed by pyrolysis. The $LiFePO_4$ crystallites in the inner part of the skeletons are therefore easily oxidized owing to air flow through the pores. On the other hand, when the sample skeletons are composed of only $LiFePO_4$ crystallites like the sample calcined at 900 °C, the crystallites in the inner part of the skeletons are harder to oxidize. A local elevation of the temperature by the burnoff of carbons may be another reason why the $LiFePO_4$ crystallites are rapidly oxidized in the samples including the large amount of carbons. Figure 12b reveals that the carbon content in the $LiFePO_4$/carbon composites can be controlled by varying the amount of PVP in the starting composition of the green bodies as expected.

3.3. Electrochemical Analysis of $LiFePO_4$/Carbon Composites. Electrochemical measurements have been carried out using a three-electrode cell to test the electrical properties of the obtained $LiFePO_4$/carbon composites. Parts a and b of Figure 13 show the first charge and discharge curves and the

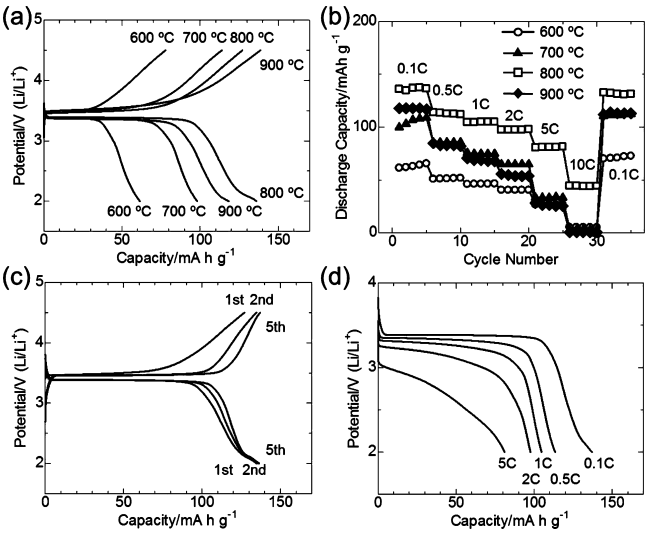

Figure 13. (a) First charge and discharge curves and (b) discharge capacities at different *C* rates of the $LiFePO_4$/carbon composite calcined at different temperatures. (c) First, second, and fifth charge and discharge curves of the sample calcined at 800 °C. (d) Discharge curves of the sample calcined at 800 °C at different *C* rates.

discharge capacities at different *C* rates of the $LiFePO_4$/carbon composite calcined at different temperatures, respectively. The *C* rates were normalized by the mass of $LiFePO_4$, which was calculated using the TG results, as shown in Figure 12. The result reveals that the sample calcined at 800 °C exhibited the best performance. With increasing calcination temperature, the electrochemical performance increased except for the sample calcined at 900 °C because of the enhancement of the crystallinity of $LiFePO_4$ as well as the development of the carbonaceous structure, which increases the conductivity of $LiFePO_4$/carbon composites. On the contrary, when the sample was calcined at 900 °C, the carbon content decreased and the dispersity of $LiFePO_4$ and carbons became poor, as shown in Figures 9 and 12. In addition, the $LiFePO_4$ crystallite size in the sample at 900 °C became larger compared to the other calcined samples, as shown in Table 2. Hence, the sample calcined at 800 °C exhibited a better performance than that at 900 °C. For the same reason, when the *C* rate increased, the discharge capacity of the sample calcined at 900 °C decreased more steeply compared to the capacity of the sample calcined at 700 °C. Figure 13c shows the first, second, and fifth charge and discharge curves of the sample calcined at 800 °C. It is found in the charge and discharge curves that the 3.5 and 3.4 V plateaus, respectively, retained the higher capacity at each time. This tendency was observed in all of the samples calcined at different temperatures. This is because the electrolyte permeated the porous active materials in the cathode better with increasing cycles.[20] The discharge curves of the sample calcined at 800 °C at different *C* rates are shown in Figure 13d. The discharge capacity decreased with increasing *C* rates, whereas the well-defined

dx.doi.org/10.1021/cm2021438 | *Chem.Mater.* 2011, 23, 5208–5216

voltage plateau remained up to 1C. However, there is no voltage plateau observed at 5C. In order to improve this tendency, a better electric conductivity and a smaller $LiFePO_4$ crystallite size are needed. Improvement of the electric conductivity can be attained by increasing the carbon content in $LiFePO_4$/carbon composites. Reduction of the crystallite size seems to be difficult but may be achieved by increasing the amount of polymers; the crystal growth during calcination can be inhibited when the crystal cores with the small size are well-covered with polymers or carbons. There may be a better carbon precursor to effectively make the nanoscale mixture of inorganic and polymer domains.

The $LiFePO_4$/carbon monoliths reported by Doherty et al. exhibited similar discharge capacities.[23] However, the 3.4 V voltage plateau in the discharge curve dropped at the smaller capacity because of the poor degree of mixing of $LiFePO_4$ and carbon. In our monolithic $LiFePO_4$/carbon composites, the macroporous structure and degree of mixing of $LiFePO_4$ and carbon have been remarkably improved. Another notable achievement of this work is that only two processes, the simple sol−gel process and calcination, give rise to the $LiFePO_4$/carbon monoliths. Furthermore, the pore characteristics, such as the macropore size, porosity, and carbon content, can be controlled simply by varying the starting composition, which enables one to improve the electrochemical performance of the material.

4. CONCLUSIONS

Monolithic $LiFePO_4$/carbon composites with well-defined macropores have been successfully fabricated by a remarkably simple two-step process: the sol−gel process followed by calcination. The precursor inorganic−organic hybrid gels, which consist of amorphous $FePO_4$ and polymers including Li ions, were prepared by the epoxide-mediated sol−gel method accompanied by spinodal decomposition. The Fe^{III} ions are simultaneously reduced into Fe^{II} with decomposition of organic volatiles and with removal of excess Cl^- ions. Hence, despite starting from iron(III) salt, the $LiFePO_4$/carbon composites can be obtained by calcination simply under a N_2 atmosphere and not under a reductive atmosphere. The resultant monolithic $LiFePO_4$/carbon composites possessed the well-defined interconnected macroporous structure as well as the smaller macropores in the skeletons that form the macroporous structure. In the composites, $LiFePO_4$ crystallites and carbons were well-mixed on the order of a 100 nm scale.

Electrochemical tests of the composite monoliths calcined at 800 °C show discharge capacities for $LiFePO_4$ of 137 mAh g^{-1} at 0.1C and 104 mAh g^{-1} at 1C. Because the various features of the $LiFePO_4$/carbon composites can be controlled as described above, it is expected that further improvements to the electrochemical performance will be achieved by optimization of the starting composition in the future. Furthermore, the synthesis method reported here is promising as a versatile technique to prepare monolithic inorganic material/carbon composites with macroporosity, which are useful for electrochemical applications.

■ ASSOCIATED CONTENT

Ⓢ Supporting Information

SEM images of the precursor gels, elemental analysis (EDX) results, and XRD patterns of the calcined samples. This material is available free of charge via the Internet at http://pubs.acs.org.

■ AUTHOR INFORMATION

Corresponding Author

*Tel/Fax: +81 757 537 673. E-mail: h_george@kuchem.kyoto-u.ac.jp.

■ ACKNOWLEDGMENTS

The present work was supported by Grants-in-Aid for Scientific Research (Grant 22-75 for G.H., Grant 22750203 for K.K., and Grant 20350094 for K.N.) from the Ministry of Education, Culture, Sports, Science and Technology (MEXT), Japan. Also acknowledged is the Global COE Program "International Center for Integrated Research and Advanced Education in Materials Science" (No. B-09) of the MEXT, Japan, administrated by the Japan Society for the Promotion of Science.

■ REFERENCES

(1) Megahed, S.; Scrosati, B. *J. Power Sources* **1994**, *51*, 79.
(2) Scrosati, B. *Nature* **1995**, *373*, 557.
(3) Tarascon, J.-M.; Armand, M. *Nature* **2001**, *414*, 359.
(4) Kang, K.; Meng, Y. S.; Bréger, J.; Grey, C. P.; Ceder, G. *Science* **2006**, *311*, 977.
(5) Whittingham, M. S. *Chem. Rev.* **2004**, *104*, 4271.
(6) Cheng, F.; Liang, J.; Tao, Z.; Chen, J. *Adv. Mater.* **2011**, *23*, 1695.
(7) Padhi, A. K.; Nanjundaswamy, K. S.; Goodenough, J. B. *J. Electrochem. Soc.* **1997**, *144*, 1188.
(8) Yamada, A.; Chung, S. C.; Hinokuma, K. *J. Electrochem. Soc.* **2001**, *148*, A224.
(9) Huang, H.; Yin, S.-C.; Nazar, L. F. *Electrochem. Solid-State Lett.* **2001**, *4*, A170.
(10) Hu, Y.; Doeff, M. M.; Kostecki, R.; Fiñones, R. *J. Electrochem. Soc.* **2004**, *151*, A1279.
(11) Delacourt, C.; Poizot, P.; Levasseur, S.; Maquelier, C. *Electrochem. Solid-State Lett.* **2006**, *9*, A352.
(12) Doeff, M. M.; Hu, Y.; McLarnon, F.; Kostecki, R. *Electrochem. Solid-State Lett.* **2003**, *6*, A207.
(13) Hsu, K.-F.; Tsay, S.-Y.; Hwang, B.-J. *J. Mater. Chem.* **2004**, *14*, 2690.
(14) Dominko, R.; Bele, M.; Gaberscek, M.; Remskar, M.; Hanzel, D.; Pejovnik, S.; Jamnik, J. *J. Electrochem. Soc.* **2005**, *152*, A607.
(15) Zhang, W.-J. *J. Electrochem. Soc.* **2010**, *157*, A1040.
(16) Chung, S.-Y.; Bloking, J. T.; Chiang, Y.-M. *Nat. Mater.* **2002**, *1*, 123.
(17) Kang, B.; Ceder, G. *Nature* **2009**, *458*, 190.
(18) Long, J. W.; Dunn, B.; Rolison, D. R.; White, H. S. *Chem. Rev.* **2004**, *104*, 4463.
(19) Fu, L. J.; Liu, H.; Li, C.; Wu, Y. P.; Rahm, E.; Holze, R.; Wu, H. Q. *Prog. Mater. Sci.* **2005**, *50*, 881.
(20) Dominko, R.; Bele, M.; Gaberscek, M.; Remskar, M.; Hanzel, D.; Goupil, J. M.; Pejovnik, S.; Jamnik, J. *J. Power Sources* **2006**, *153*, 274.
(21) Wang, Y.; Cao, G. *Adv. Mater.* **2008**, *20*, 2251.
(22) Doherty, C. M.; Caruso, R. A.; Smarsly, B. M.; Drummond, C. J. *Chem. Mater.* **2009**, *21*, 2895.
(23) Doherty, C. M.; Caruso, R. A.; Smarsly, B. M.; Adelhelm, P.; Drummond, C. J. *Chem. Mater.* **2009**, *21*, 5300.
(24) Qian, J.; Zhou, M.; Cao, Y.; Ai, X.; Yang, H. *J. Phys. Chem. C* **2010**, *114*, 3477.
(25) Tokudome, Y.; Fujita, K.; Nakanishi, K.; Miura, K.; Hirao, K. *Chem. Mater.* **2007**, *19*, 3393.
(26) Tokudome, Y.; Nakanishi, K.; Kosaka, S.; Kariya, A.; Kaji, H.; Hanada, T. *Microporous Mesoporous Mater.* **2010**, *132*, 538.
(27) Tokudome, Y.; Miyasaka, A.; Nakanishi, K.; Hanada, T. *J. Sol−Gel Sci. Technol.* **2011**, *57*, 269.
(28) Itoh, H.; Tabata, T.; Kokitsu, M.; Okazaki, N.; Imizu, Y.; Tada, A. *J. Ceram. Soc. Jpn.* **1993**, *101*, 1081.
(29) Gash, A. E.; Tillotson, T. M.; Satcher, J. H. Jr.; Hrubesh, L. W.; Simpson, R. L. *J. Non-Cryst. Solids* **2001**, *285*, 22.

(30) Gash, A. E.; Tillotson, T. M.; Satcher, J. H. Jr.; Poco, J. F.; Hrubesh, L. W.; Simpson, R. L. *Chem. Mater.* **2001**, *13*, 999.
(31) Nakanishi, K. *J. Porous Mater.* **1997**, *4*, 67.
(32) Maiyalagan, T.; Viswanathan, B. *Mater. Chem. Phys.* **2005**, *93*, 291.
(33) Barker, J.; Saidi, M. Y.; Swoyer, J. L. *Electrochem. Solid-State Lett.* **2003**, *6*, A53.
(34) Kim, C. W.; Lee, M. H.; Jeong, W. T.; Lee, K. S. *J. Power Sources* **2005**, *146*, 534.
(35) Iuliano, M.; Ciavatta, L.; Tommaso, G. D. *Soil Sci. Soc. Am. J.* **2007**, *71*, 1137.
(36) Pigeon, M.; Prud'homme, R. E.; Pézolet, M. *Macromolecules* **1991**, *24*, 5687.
(37) Julien, C. M.; Zaghib, K.; Mauger, A.; Massot, M.; Ait-Salah, A.; Selmane, M.; Gendron, F. *J. Appl. Phys.* **2006**, *100*, 063511.
(38) Erdemi, H.; Bozkurt, A. *Eur.—Polym. J.* **2004**, *40*, 1925.
(39) Daheron, B.; MacNeli, D. D. *J. Solid State Electrochem.* **2011**, *15*, 1217.
(40) Tennison, S. R. *Appl. Catal., A* **1998**, *173*, 289.